European Journal of Environmental and Civil Engineering

ISSN: (Print) (Online) Journal homepage: https://www.tandfonline.com/loi/tece20

Experimental and numerical investigation of hyper-elastic submerged structures strengthened with cable under seismic excitations

A. Ersin Dinçer

To cite this article: A. Ersin Dinçer (2020): Experimental and numerical investigation of hyper-elastic submerged structures strengthened with cable under seismic excitations, European Journal of Environmental and Civil Engineering, DOI: 10.1080/19648189.2020.1837253

To link to this article: https://doi.org/10.1080/19648189.2020.1837253

Published online: 23 Oct 2020.

EUROPEAN JOURNAL OF ENVIRONMENTAL AND CIVIL ENGINEERING
https://doi.org/10.1080/19648189.2020.1837253

Experimental and numerical investigation of hyper-elastic submerged structures strengthened with cable under seismic excitations

A. Ersin Dinçer

Department of Civil Engineering, Hydraulics Laboratory, Abdullah Gül University, Kayseri, Turkey

ABSTRACT

This study presents dynamic responses of submerged highly elastic structures, strengthened with cable elements and the fluid interacting with the structure. For this purpose, fluid and structure are modelled with smoothed particle hydrodynamics and finite element methods, respectively. The interaction is satisfied with contact mechanics. In order to simulate the cable, a finite element model with a two-node cable element is used. The stiffness obtained from the cable is added to the structure and the whole fluid-structure system is solved together. The novel contribution of the present study is the coupling a two-node cable element model with the fluid-structure interaction method. In order to validate the numerical method, a set of novel experiments is carried out. In the experiments, cable elements are attached to an elastic structure that is placed in a water tank. Near-fault and earthquake excitations are applied to the tank and the displacement of the structure and the free surfaces of the water are recorded. All the results show that the proposed two-dimensional numerical model is capable of modelling the submerged elastic structure strengthened with the cable under the seismic excitations.

ARTICLE HISTORY
Received 30 May 2020
Accepted 10 October 2020

KEYWORDS
Smoothed particle hydrodynamics; cable; moorings; fluid-structure interaction; submerged elastic structure; computational fluid dynamics

Introduction

Analysis of hyper-elastic structures is difficult due to high nonlinearity causing very large deformations (Kim et al., 2001). If these structures are submerged, the analysis becomes much harder because of the continuous interaction with the fluid. An example of these structures can be a submerged minaret of a mosque. Since many of the submerged structures are historical such as the ruins of Halfeti, whose foundation dates back to ninth century and located in the southeastern of Tukey, strengthening of the structures becomes more important. The easiest way to protect the structures from the seismic excitations is to assemble cable elements that decrease the deformation. Although strengthening of these structures with cable elements may decrease the deformation, the complexity of the problem increases. A suitable numerical or experimental model is required to analyse submerged hyper-elastic structures strengthening with cable elements.

There are some recent studies related to the submerged structures. The flexibility of an elastic submerged structure was investigated with the coupling of boundary element and finite element methods in Ghalandari et al. (2019). The flows over rigid submerged vegetation were investigated in Wai Li and Busari (2019). Although there are no studies investigating the behaviour of a submerged elastic structure having a cable element, offshore structures whose dynamic response is controlled by cable elements

CONTACT A. Ersin Dinçer ersin.dincer@agu.edu.tr Department of Civil Engineering, Hydraulics Laboratory, Abdullah Gül University, Kayseri 38080, Turkey

have been studied in the literature. Offshore structures such as offshore wind farms or offshore oil platforms are floating on the sea surface and a mooring system, any type of cable, fibre rope, wire or chain that connects a floating platform to an anchoring system fixed at the sea floor (Davidson & Ringwood, 2017) is used to limit their motions. To simulate cable elements different type of models have been proposed such as: closed form solution (Orgill et al., 1985), finite-element models (Fogazzi & Perotti, 2000; Zhu et al., 2013) and lumped-mass method (Nakajima, 1982).

In a recent study, the behaviour of the mooring floating objects was numerically investigated by modelling mooring with a closed form catenary function (Barreiro et al., 2016). The fluid was modelled with smoothed particle hydrodynamics (SPH), a Lagrangian particle method and rigid body dynamics was used to simulate the floating object. The same method was also applied to simulate the offshore oscillating water column converters with mooring systems (Crespo et al., 2017). The main drawback of the method is modelling the mooring with a catenary equation which may not provide accurate results for nonlinear problems (Cui et al., 2019). To overcome this problem, lumped-mass method was used to model mooring by keeping the simulation method of the fluid and the solid bodies the same with the former study (Cui et al., 2019). In a different study, the mooring was taken as a light spring and the calculated force and the torque of the mooring were transmitted to the solid floating body (Ren et al., 2017). In the aforementioned studies, solid was assumed as rigid. Although this assumption may be correct for floating offshore structures, it does not include the elasticity of the solid body, so it cannot be used for the elastic submerged structures.

The problem domain of a submerged elastic structure with a cable element includes fluid, solid and cable parts. Traditional computational fluid dynamics (CFD) techniques may be used to simulate the fluid (Akbarian et al., 2018; Rebouillat & Liksonov, 2010). However, extensive mesh generation is usually required in Eulerian mesh-based techniques. Therefore, Lagrangian mesh-free techniques have become popular especially for the problems having free surfaces. Amongst them SPH is one of the most popular Lagrangian particle methods. It was first introduced by Gingold and Monaghan (Gingold & Monaghan, 1977) and Lucy (Lucy, 1977) for astrophysical problems and then applied to many fields such as free-surface (Monaghan, 1994), closed-conduit (Dinçer, 2017; Dinçer et al., 2018) and multiphase (Calderer et al., 2014) flows, solid mechanics (Cyril et al., 2019), geomechanics (Blanc & Pastor, 2011), fluid sloshing (Shao et al., 2012), fluid-structure interaction (FSI) problems (Antoci et al., 2007; Demir et al., 2019; Dinçer et al., 2019; Yang et al., 2012), etc.

SPH is superior to deal with the problems having large deformations or free surfaces. On the other hand, for the simulation of the solid, finite element (FE) method is superior in terms of accuracy and stability. Therefore, in the present study, the behaviour of a submerged elastic structure with a cable element under seismic excitations is investigated by simulating fluid and structure with SPH and finite element methods, respectively. The coupling of fluid and solid domains is satisfied with contact mechanics which is the main difference from the previous SPH-FE methods. Numerical instabilities may be observed when contact mechanics is used as the interaction method. In order to prevent these instabilities, shifting the surface of the structural domain (SSOSD) is used. In SSOSD, an intermediate boundary layer between fluid and structure domains is defined. The fluid particles in this domain are repositioned based on an exponential function. Since the particles are allowed to stay within the intermediate domain, the forces on the particles due to contact mechanics algorithm are more uniform (Dinçer et al., 2019). The novel contribution of the numerical model in the present study is that a finite element model with a two-node cable element is integrated with a recently developed fully coupled SPH-FE method. In the model, the interaction between the water and the cable is assumed as negligible. Numerical results are validated with novel experimental studies. In the experimental studies, a submerged hyper-elastic plate or simply rubber, is placed in the middle of a tank filled with water. Highly elastic cable elements are attached to the rubber. By applying near-fault and earthquake excitations, the top displacements of the rubber and free-surface profiles of fluid are measured and compared with the numerical data. As far as the author's best knowledge, this is the first study in which a comprehensive finite-element cable model is incorporated with SPH-FEM FSI method in which highly elastic structure is in interaction with the fluid. Besides, the behaviour of a highly deformable structure with a cable element under near-fault and earthquake excitations has never been investigated before. Additionally, the experiments conducted to validate the numerical model are novel.

The paper is organised as follows:

i. first SPH, coupling mechanism of SPH and FE and the implementation of cable are described in Section 2,
ii. the experimental setup is described in Section 3.
iii. Section 4 is dedicated to the comparison of the numerical model with experiments
iv. conclusions are drawn in Section 5.

2. Numerical models

2.1. Smoothed particle hydrodynamics

For a weakly compressible and barotropic fluid, Navier-Stokes equations can be shown in Lagrangian form as:

$$\frac{D\rho}{Dt} = -\rho\nabla\cdot\boldsymbol{u} \tag{1}$$

$$\rho\frac{D\boldsymbol{u}}{Dt} = -\nabla p + \mu\nabla^2\boldsymbol{u} + \rho\boldsymbol{g} \tag{2}$$

where ρ, $\boldsymbol{u}$ and $\boldsymbol{g}$ represent density of the fluid, flow velocity vector and gravitational acceleration vector, respectively. p denotes the pressure and μ denotes the dynamic viscosity of the fluid.

In the study, instead of density filtering technique (Colagrossi & Landrini, 2003) which violates the conservation of the total volume of the particles (Antuono et al., 2010), δ-SPH model is used due to its superiority on the problems having violent free-surface flows (Marrone et al., 2011). In δ-SPH model, numerical diffusive terms are added to the governing equations to decrease the numerical oscillations in pressure field. The governing Navier-Stokes equations in δ-SPH scheme can be represented as:

$$\frac{D\rho_i}{Dt} = \sum_j m_j(\boldsymbol{u}_j - \boldsymbol{u}_i)\cdot\nabla_i W_{ij} + \delta hc_0\sum_j \varphi_{ij}\cdot\nabla_i W_{ij} \tag{3}$$

$$\rho_i\frac{d\boldsymbol{u}_i}{dt} = -\sum_j m_j(p_i + p_j)\nabla_i W_{ij} + \rho_i\mathbf{g}_i + \alpha hc_0\rho_0\sum_j \pi_{ij}\frac{m_j}{\rho_j}\nabla_i W_{ij} + \Delta\boldsymbol{C} \tag{4}$$

$$\varphi_{ij} = 2(\rho_j - \rho_i)\frac{\boldsymbol{r}_{ji}}{|\boldsymbol{r}_{ij}|^2} - \left[\nabla\rho_i^{\,L} + \nabla\rho_j^{\,L}\right] \tag{5}$$

where m is the mass of a fluid particle, δ and α are coefficients to control the intensity of diffusion of density and velocity, respectively. In the simulations, as proposed in Marrone et al. (2011), δ and α are taken as 0.1 and 0.02, respectively. c_0 is the speed of sound and assumed to be constant throughout the simulation. W_{ij} is the kernel function. At first Gaussian kernel function was introduced into the SPH, but cubic spline kernel is the most common one in SPH method (Gomez-Gesteira et al., 2010; Liu & Liu, 2010). Lately, Wendland kernel function (Dehnen & Aly, 2012) has become popular in SPH simulations (Cao et al., 2014). In the present study, cubic spline kernel with a smoothing length equals to 1.33 times the initial spacing between the particles and a support of radius equal to 2 times the smoothing length is used. Since the first derivative of the cubic spline kernel goes to zero, a well-known tensile instability problem resulting in particle clustering may be observed. To prevent tensile instability, the correction method proposed in Monaghan (2000) is adopted. $\Delta\boldsymbol{C}$ is the acceleration vector due to the contact force exerted by the structure. $\nabla\rho^L$ is the renormalised density gradient and calculated by,

$$\langle\nabla\rho\rangle_i^{\,L} = \sum_j \frac{m_j}{\rho_j}(\rho_j - \rho_i)\boldsymbol{L}_i\nabla_i W_{ij} \tag{6}$$

$$\boldsymbol{L}_i = \left[\sum_j \frac{m_j}{\rho_j}\boldsymbol{r}_{ij}\otimes\nabla_i W_{ij}\right]^{-1} \tag{7}$$

where $\boldsymbol{r}_{ij}$ is the difference of the position vectors between particles i and j.

π_{ij} is the artificial viscosity term to be used both to stabilise the numerical scheme and to mimic the real viscosity and can be calculated as (Monaghan, 1994):

$$\pi_{ij} = \frac{(\boldsymbol{u}_j - \boldsymbol{u}_i) \cdot \boldsymbol{r}_{ji}}{|\boldsymbol{r}_{ij}|^2} \tag{8}$$

When the fluid is assumed to be incompressible, Poisson's equations should be solved resulting the higher computational time (incompressible SPH – ISPH). To avoid solving Poisson's equations, weakly compressible SPH model is used. According to the weakly compressible SPH assumption, the pressure of a particle is calculated by:

$$p_i = {c_0}^2(\rho_i - \rho_0) \tag{9}$$

where ρ_0 is the initial density. In order to satisfy weakly compressible assumption, density variations are kept below 1%. Therefore, speed of sound should be used much lower than that of the real fluid. According to Morris et al. (1997), the square of the speed of sound should be compatible with the following equation:

$$c^2 = max\left({u_b}^2 \frac{\rho_0}{\Delta\rho}, \quad \frac{\mu u_b}{\rho l}\frac{\rho_0}{\Delta\rho}, Fl\frac{\rho_0}{\Delta\rho}\right) \tag{10}$$

where F is the magnitude of external force, l is the length scale, u_b is the fluid bulk velocity, $\Delta\rho$ is the absolute density variation. In order to ensure the neighbouring particles to move with closer velocities, the XSPH correction can be used (Monaghan, 1994).

$$\frac{d\boldsymbol{r}_i}{dt} = \boldsymbol{u}_i + 0.05\sum m_j\left(\frac{\boldsymbol{u}_i - \boldsymbol{u}_j}{\overline{\rho}_i}\right)W_{ij} \tag{11}$$

Leap frog algorithm is used to integrate the differential equations due to its computational efficiency and the requirement of less memory (Liu & Liu, 2003). Courant-Friedrichs-Lewy (CFL) stability condition is adopted to define the maximum time step in the simulation (Anderson, 1995).

To simulate the walls two types of boundaries have been used in SPH literature. In the first type, walls are filled with the particles, so the kernel support for a fluid particle near a wall is completed. In the second method, particles are placed on the wall and an artificial repulsive force is applied to the fluid particles. The magnitude of the force increases whilst a fluid particle is approaching to the boundary. Hybrid methods are also available in which both boundary treatments are used (Shao et al., 2012).

In the first method, ghost particles, the mirror images of fluid particles along the surface, are created. Dealing with the complex boundaries and high computational time are the two limitations of this boundary type (Morris et al., 1997). To deal with these limitations some remedies have been proposed. For example, a correction to the ghost particle method was proposed to deal with the complex geometries (Adami et al., 2012). Fixed ghost particle technique in which ghost particles are created at the beginning of the simulation and the positions of them are not modified at every time step were also used in Marrone et al. (2011).

In the second method, single layer of boundary particles is created at the beginning of the simulation, so dealing with the complex geometries is easier. The hydrodynamic properties of the boundary particles are modified at each time step. Since the boundary particles are not created at every time step, the computational efficiency is higher. The main problem of this boundary method is that kernel support of fluid particles near the walls is not completed, so kernel truncation error is observed.

In the present study, the boundary method proposed in Monaghan and Kos (1999) is adapted in the regions where the deformation of the structure is not important. According to the method, when a fluid particle approaches a boundary particle, a force is exerted to the fluid particle. Local unit normal vectors from boundary to the fluid should be defined at the beginning of the simulations so that a force normal to the boundary is produced from the boundary particles.

A different type of boundary should be implemented in the regions where the structural deformation is important. To represent this boundary, contact mechanics previously proposed by the author is used (Dinçer et al., 2019). The mechanism of contact mechanics and the application to the SPH-FE method were explained in detail in the previous studies (Demir et al., 2019; Dinçer et al., 2019) and a brief explanation is given in the coupling algorithm part of the present study. In contact mechanics, the velocity component in local tangential direction of a particle near the boundary is zero, so the parallel movement of SPH particles is not disturbed.

2.2. Cable

A two-node cable element is used to solve catenary cable considering nonlinear geometric effects (Yang & Tsay, 2007). In the two-node cable element, each cable of a cable-supported structure can be modelled by a single or a small number of elements. The horizontal and the vertical equilibrium conditions of the cable can be determined as:

$$T\frac{dx}{ds} = T_x \tag{12}$$

$$T\frac{dy}{ds} = T_y - m_c g s_0 \tag{13}$$

where T is tension of the cable, T_x and T_y are directional components of tension of the cable, m_c is the mass of the cable per unit length, s_0 and s are unstretched and stretched lengths of the portion of the cable measured from the support, respectively. The cable tension and the coordinates can be determined from the Equations (12) and (13).

$$T(s_0) = \sqrt{{T_x}^2 + (T_y - m_c g s_0)^2} \tag{14}$$

$$x(s_0) = \frac{T_x s_0}{EA} + \frac{T_x}{m_c g}\left[\sinh^{-1}\left(\frac{T_y}{T_x}\right) - \sinh^{-1}\left(\frac{T_y - m_c g}{T_x}\right)\right] \tag{15}$$

$$y(s_0) = \frac{m_c g L_0 s_0}{EA}\left(\frac{T_y}{m_c g L_0} - \frac{s_0}{2L_0}\right) + \frac{T_x}{m_c g}\left[\sqrt{1 + \left(\frac{T_y}{T_x}\right)^2} - \sqrt{1 + \left(\frac{T_y - m_c g s_0}{T_x}\right)^2}\right] \tag{16}$$

where E is the elasticity modulus of the cable and A is the cross-sectional area of the cable in unstretched profile. By applying boundary conditions of $x(0) = 0$, $y(0) = 0$, $x(L_0) = l$ and $y(L_0) = h$, the vertical, h, and horizontal, l, projection lengths of the cable can be found. Using the relation between tension components and projection lengths, flexibility matrix, $\boldsymbol{flx}$, can be determined.

$$\begin{Bmatrix} dl \\ dh \end{Bmatrix} = \begin{bmatrix} flx_{11} & flx_{12} \\ flx_{21} & flx_{22} \end{bmatrix} \begin{Bmatrix} dT_x \\ dT_y \end{Bmatrix} \tag{17}$$

where components of the flexibility matrix can be determined as follows:

$$flx_{11} = \frac{L_0}{EA} + \frac{1}{m_c g}\left[\sinh^{-1}\left(\frac{T_y}{T_x}\right) - \sinh^{-1}\left(\frac{T_y - m_c g L_0}{T_x}\right)\right] + \frac{1}{m_c g}\left[-\frac{T_y}{T(0)} - \frac{T_y - m_c g L_0}{T(s_0)}\right] \tag{18a}$$

$$flx_{12} = \frac{1}{m_c g}\left[-\frac{T_x}{T(0)} - \frac{T_x}{T(s_0)}\right] \tag{18b}$$

$$flx_{21} = \frac{{flx_{12}}^{-1}}{(m_c g)^2} + \frac{1}{m_c g {T_x}^2}\left[-\frac{T_x {T_y}^2}{T(0)} + \frac{T_x (T_y - m_c g L_0)^2}{T(s_0)}\right] \tag{18c}$$

$$flx_{22} = \frac{L_0}{EA} + \frac{1}{m_c g}\left[-\frac{T_y}{T(0)} - \frac{T_y - m_c g L_0}{T(s_0)}\right] \tag{18d}$$

The stiffness matrix of the cable, $\boldsymbol{K}_{cable}$, is the inverse of the defined flexibility matrix. In order to represent the stiffness matrix in the global coordinate system, it should be multiplied with a transformation matrix. In the present study, the interaction between the cable and fluid is ignored.

2.3. Coupling algorithm

In FSI problems, interface between fluid and structure should be treated correctly for all coupled methods. Contact mechanics is used to eliminate the invasion of fluid particles of the solid domain. Contact mechanics is usually preferred to simulate the contact between two solid bodies. It was first applied to a fluid-structure interaction problem in a recent study (Dinçer et al., 2019). The first advantage of contacts mechanics may be the elimination of predictive corrective steps so that the completeness of the whole system is guaranteed. Second, a continuous boundary is achieved since master nodes or SPH particles

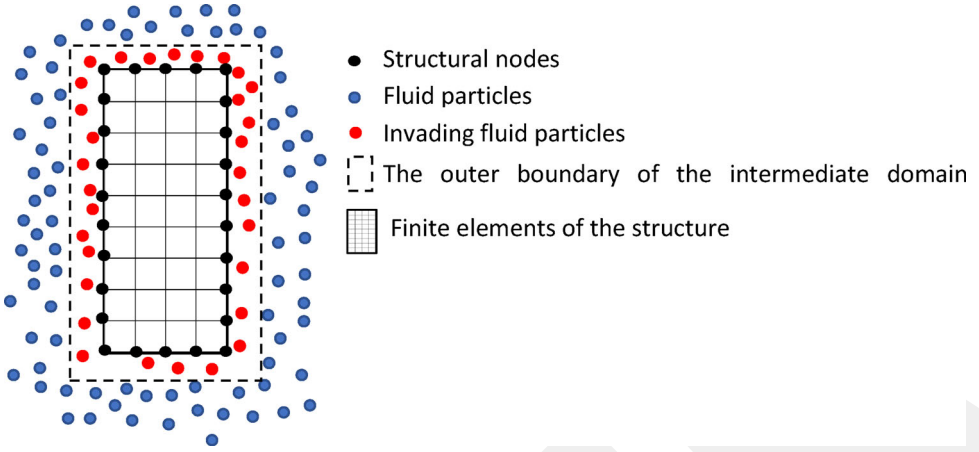

Figure 1. Interface between fluid and structure.

are not defined on the boundary. Third, a uniform tangential force is applied from the boundary to the SPH particles. In Figure 1, the interface between fluid particles and structural elements is shown. An intermediate boundary layer is defined in the fluid domain located at the surface of structural domain and fluid particles inside this domain are relocated based on a predefined nonlinear function. In order to relocate the particles, an exponential function is used. SPH particles are allowed to stay within the intermediate boundary layer whilst exposed to displacements. The method is called (SSOSD) and the formulations of contact mechanics and SSOSD are given below.

As can be seen in Figure 1, there is a deformable body and a number of fluid particles in an FSI problem. In the proposed method, SPH particles invading the structural domain are repelled by solving the contact mechanics equations derived below. In contact mechanics, a contact potential should be defined before calculating the contact force. A two-dimensional node to line (in this case particle to line) contact potential due to the invasion of the solid domain can be stated as (Bathe & Chaudhary, 1985; Demir et al., 2019):

$$\Pi_{inv} = \left(\boldsymbol{C}_{inv}^{t+\Delta t} + \Delta \boldsymbol{C}_{inv}\right)^{T} \left[(\Delta \boldsymbol{u}_{inv} + \boldsymbol{O}_{inv}) - (1-\eta)\Delta \boldsymbol{u}_{F} - \eta \Delta \boldsymbol{u}_{S}\right] \tag{19}$$

where *inv* denotes the invader particle and superscripts denote time, $\boldsymbol{C}_{inv}$ is the contact force, $\Delta \boldsymbol{u}_{inv}$, $\boldsymbol{O}_{inv}$ are the incremental displacement and overlap of invader particle, respectively. $\Delta \boldsymbol{u}_{F}$ and $\Delta \boldsymbol{u}_{S}$ are the incremental displacement of the first and the second nodes of line element, respectively. η is a parameter defining the position of contact point from the first node of line element and can be calculated from the following equation:

$$\eta = \frac{\boldsymbol{n}}{l_e}^{T} \left[\left(\boldsymbol{r}_{inv}^{t+\Delta t} - \boldsymbol{O}_{inv}^{t+\Delta t}\right) - \boldsymbol{r}_{F}^{t+\Delta t}\right] \tag{20}$$

where $\boldsymbol{n}$ is the unit normal vector of the line element, l_e is the length of the line element, $\boldsymbol{r}_{inv}$ and $\boldsymbol{r}_{F}$ are the position vectors of the particle and node, respectively.

By subtracting the summation of the contact potential of the invader particles from the existing potential, incremental finite element equations with contact conditions are obtained.

$$\begin{bmatrix} \boldsymbol{K}_{solid}^{t+\Delta t} + \boldsymbol{K}_{cable}^{t+\Delta t} & \boldsymbol{K}_{c}^{t+\Delta t} \\ \left(\boldsymbol{K}_{c}^{t+\Delta t}\right)^{T} & 0 \end{bmatrix} \begin{bmatrix} \Delta \boldsymbol{U} \\ \Delta \boldsymbol{C}_{inv} \end{bmatrix} = \begin{bmatrix} \boldsymbol{R}^{t+\Delta t} \\ 0 \end{bmatrix} - \begin{bmatrix} \boldsymbol{F}^{t+\Delta t} \\ 0 \end{bmatrix} + \begin{bmatrix} \boldsymbol{R}_{c}^{t+\Delta t} \\ \boldsymbol{O}_{inv}^{t+\Delta t} \end{bmatrix} \tag{21}$$

where $\boldsymbol{K}_{solid}$ and $\boldsymbol{K}_{cable}$ are the stiffness matrices of solid structure and cable, respectively, $\boldsymbol{K}_{c}$ is the contact stiffness matrix, $\Delta \boldsymbol{U}$ is the incremental displacement vector, $\boldsymbol{R}$ is the total applied external load vector, $\boldsymbol{F}$ is the equivalent nodal forces vector, $\boldsymbol{R}_{c}$ is the contact force vector elements calculated by using the position of contact point defined by η.

Mass participation of invading particles is added to Equation (21) by using Newmark's method (Newmark, 1959) which is a well-known, unconditionally stable, second order method. Before the

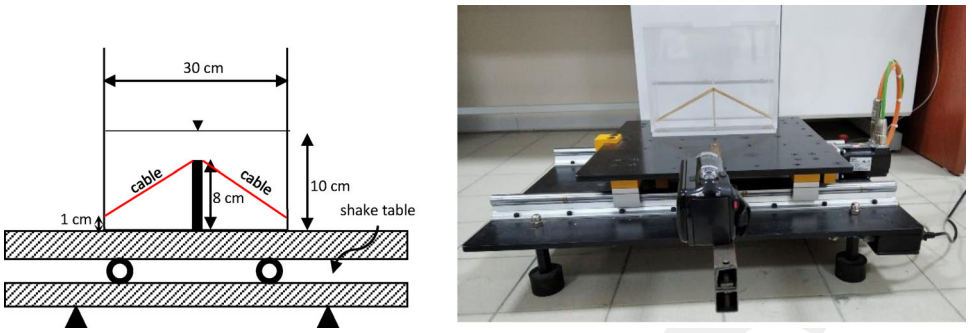

Figure 2. Experimental setup.

substitution of mass participation of invaders, mass matrix should be multiplied by $^{2}/_{\Delta t^{2}}$. A more detailed derivation can be found in a previous study of the author (Dinçer et al., 2019).

After adding mass participation, by solving Equation (21), the contact force is obtained and added to the governing equation of SPH method as shown in Equation (4).

According to SSOSD formulation, overlap vector of invader particles should be modified in accordance with the following equation.

$$\left({}_{new}\boldsymbol{O}_{inv}^{t+\Delta t}\right)_n = \left(\boldsymbol{O}_{inv}^{t+\Delta t}\right)_n - \boldsymbol{d} + e^{-\left(\left|\left(\boldsymbol{o}_{inv}^{t+\Delta t}\right)_n\right| / |\boldsymbol{d}|\right)}\boldsymbol{d} \tag{22}$$

where $\left(\boldsymbol{O}_{inv}^{t+\Delta t}\right)_n$ is the overlap of the invader particle in local normal direction $\boldsymbol{n}$ of the boundary surface. $\left({}_{new}\boldsymbol{O}_{inv}^{t+\Delta t}\right)_n$ is the modified overlap vector, $\boldsymbol{d}$ is a flow dependent vector in local normal direction $\boldsymbol{n}$. The upper and lower limits of $\boldsymbol{d}$ can be calculated from:

$$5 \leq \frac{\left|\vec{d}\right| h_0}{u_{max}\Delta t} \leq 50 \tag{23}$$

where h_0 is the initial distance between two adjacent particles assuming that the particles are placed uniformly and the horizontal and the vertical initial distances between two particles are the same. u_{max} is the magnitude of the maximum particle velocity and Δt is the time step calculated by CFL condition. Hydrodynamics variables of the particles should also be modified in accordance since the particles are shifted from the original positions found in Equation (21) according to the following equation.

$${}_{new}\omega_i = \omega_i + {}_{new}\boldsymbol{O}_{inv}^{t+\Delta t} \cdot (\nabla\omega)_i \tag{24}$$

where ω_i is a general hydrodynamic variable such as pressure, ${}_{new}\boldsymbol{O}_{inv}^{t+\Delta t}$ is the distance between the particle's old position and new position.

3. Experimental setup

A rectangular tank made of plexiglass was placed on a shake table as shown in Figure 2. A rubber was located in the middle of the tank. The rubber was fixed at its lower end and it was free at its upper end, thus representing a submerged structure. The width, length and height of the tank were 15 cm, 30 cm and 40 cm, respectively. Thickness of plexiglass was 1 cm, so the walls of the tank can be assumed as rigid. The height and the width of the rubber were 8 cm and 0.3 cm, respectively. The elastic modulus of the rubber was measured in the laboratory and an average value of 10 MPa was decided to be used in the simulations. The rubber was supported with symmetrically placed highly elastic cables. Three cables were used to satisfy two-dimensional assumption. Although three-dimensional models are more popular with the advances in computing technology, experiments that can be considered as two-dimensional benchmark problems were conducted. Researchers may validate their two-dimensional numerical model including elastic structure and cable elements with the present experiments. The cross-sections of cables

Table 1. The parameters used in the numerical model.

The initial distance between SPH particles (cm)	0.15
The height of the plate (cm)	8.0
The width of the plate (cm)	0.3
Modulus of elasticity of the plate (MPa)	10.0
The number of SPH particles	13,146
The number of finite elements	120
Max. time step (s)	0.000016
The initial length of the cable (cm)	16.2
The modulus of elasticity of the cable (MPa)	1.14

are square having a side length of 2 mm. One end of the cables was attached to the top of the rubber, whilst the other end was attached to the left or right walls and they were placed 1 cm above the bottom of the tank. The unstretched length of a single cable was 16.2 cm. To observe the deformation of the rubber clearly and validate the numerical model, cables having small modulus of elasticity were used in the experiments. The modulus of elasticity of the cable was measured as 1.14 MPa.

The tank was partially filled with water with a depth of 10 cm. The density of water was 1000 kg/m^3. A high-resolution camera, capturing 30 fps, was fixed in the middle of the tank and it was in the same motion with the tank. The sloshing of water and the deformation of the rubber was obtained with an image processing technique.

Since the purpose of this study is to validate a newly proposed numerical algorithm, a theoretical experimental setup was chosen. The dimensions were small compared to the real case. In addition, a smaller elasticity of the cable was preferred to allow to clearly observe the tip displacements of the rubber. Although they are theoretical, the experiments may be the benchmark for the researchers who want to validate their FSI method incorporated with cable elements. All the experiments were conducted 5 times to satisfy the repeatability. It should be pointed out that the main experimental parameters are taken the same with the previous experiments in which the deformation of a submerged rubber under seismic excitations was investigated (Dinçer, 2019). The main contribution of this study is the attachment of the cable elements to the rubber.

4. Numerical results

In the numerical simulations, the initial distance between two SPH particles was taken as 1.5 mm, accordingly approximately 13,150 SPH particles were used. The number of finite elements for elastic plate was 120. The numbers of particles and finite elements were defined after a convergence analysis which is explained in the next part. Maximum time step was controlled by CFL stability condition. The initial water depth in the tank was 10 cm.

In Table 1, the parameters used in the numerical model are summarised. Initial particle and mesh distributions are shown in Figure 3. It should be pointed out that the interaction between the fluid particles on different sides of the rubber is prevented by excluding those particles from their neighbouring list in the searching algorithm.

4.1. Near-fault-type excitation

Structures may be highly damaged due to the near-fault excitations in which a high energy is transferred to the structure resulting from the impulsive character of the velocity and the ground motions of near-fault excitations (Zhang & Wang, 2013). In order to find the nonlinear behaviour of a submerged structure with cable and the sloshing of the water, the tank was applied idealised near-fault excitations as shown in Figure 4.

A convergence analysis for the rubber with cable under one-cycle cosine impulse was performed by changing the number of SPH particles and finite elements and presented in Figure 5. The left column labelled with (a) shows water level change on the right wall of the tank, whereas the right column labelled with (b) presents the horizontal tip displacements of the rubber. First, the number of finite elements was kept constant and the number of particles was changed and the change in water level on the right wall was observed. A slight change in results is observed with the increase in particle numbers

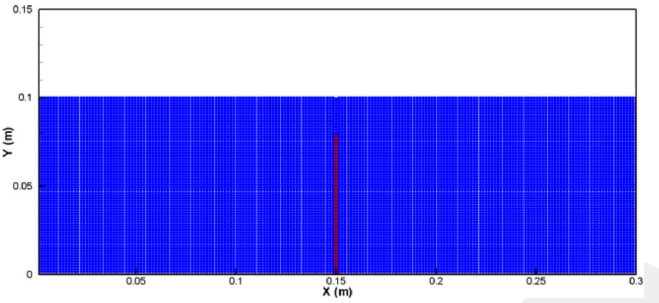

Figure 3. Initial particle and mesh distribution.

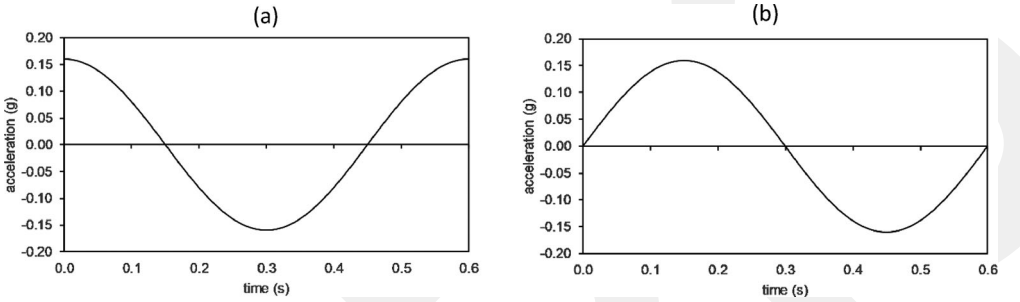

Figure 4. Idealised near-fault impulses (a) one-cycle cosine and (b) one-cycle sine.

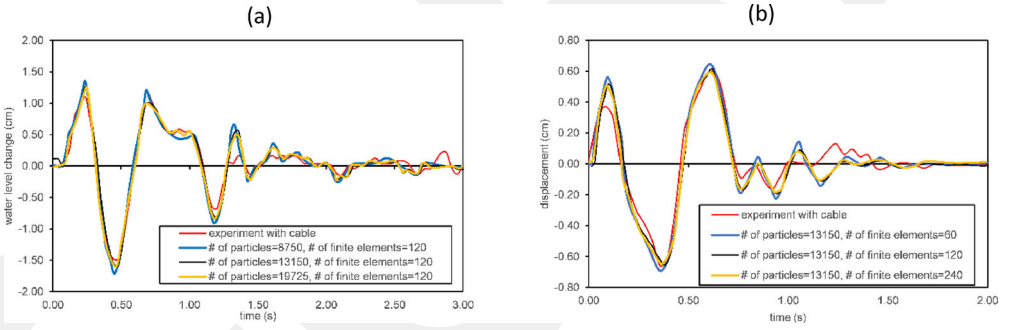

Figure 5. Convergence analysis under one-cycle cosine impulse.

from 8750 to 13,150 particles. Further increase in the number of particles do not affect the results. Similar analysis was performed by changing the number of finite elements whilst keeping the number of particles constant and the horizontal tip displacements of rubber were observed. Accordingly, 120 finite elements were decided to be used in the simulations.

Free-surface profiles at random instants under one-cycle cosine and one-cycle sine impulses can be seen in Figures 6 and 7. In the figures, the left column shows the experimental results when upper end of the rubber is free, whereas in the middle column experimental results when cable elements are attached are shown. In the right column, simulation results when cable elements are attached to the rubber are given. Numerical results when the upper end of rubber is free can be found in a previous study of the author (Dinçer, 2019). It should be noted that although the cable elements are shown in the figures for the sake of completeness, the interaction between the fluid and the cable is ignored. As seen in the figures, free-surface profiles change considerably when cable elements are attached to the rubber. In addition, the tip displacement of the rubber decreases as expected. Numerical results are similar to the experimental results, although water bubbles could not be captured in the simulations. Pressure distribution is also given in the numerical results. Since, pressures at different levels were not measured in the experiments, it is not possible to validate them. The simulated positions of cable elements at different

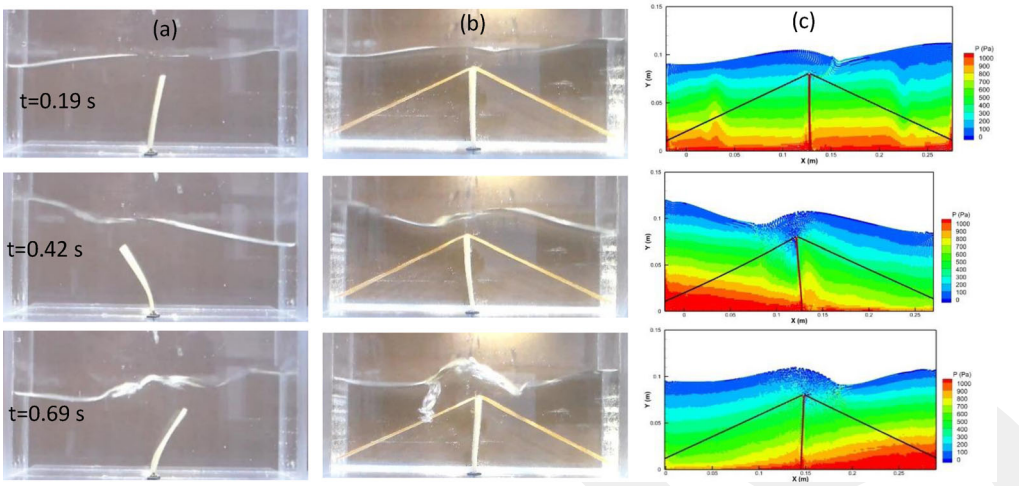

Figure 6. Free-surface profiles under one-cycle cosine impulse of (a) experiment without cable, (b) experiment with cable, (c) simulation with cable.

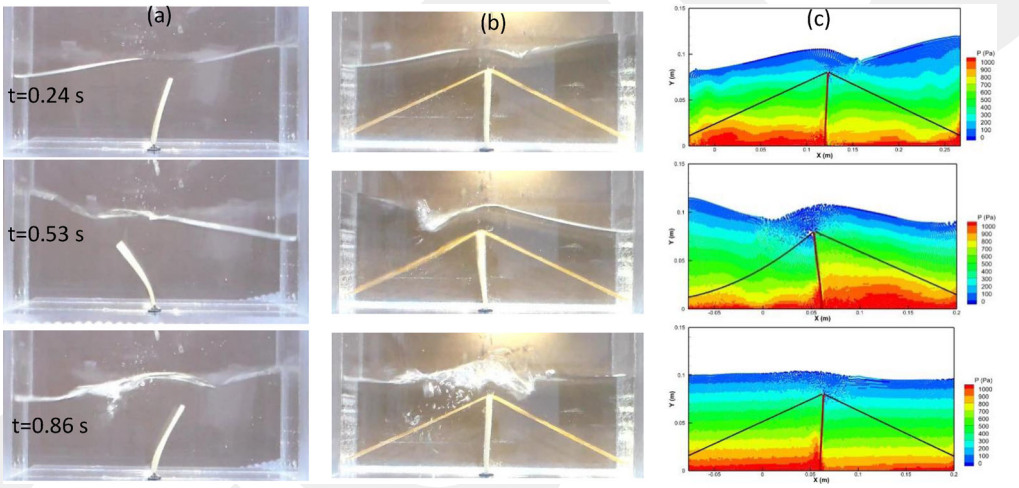

Figure 7. Free-surface profiles under one-cycle sine impulse of (a) experiment without cable, (b) experiment with cable, (c) simulation with cable.

instants are generally close to the experimental data. In Figure 7 at $t = 0.53$ s, a small sag is observed in the simulation on the cable located on the left side of the tank. The cable is not in tension, so the sag is due to its own weight. Although it is obvious in the experimental data that the same cable is not in tension, the sag is not observed in the experiments. However, the positions of three cables are not the same in the experiments as can be seen in the figure. In fact, the position of the cable not in tension does not affect SPH-FEM solution, because there is not any significant force contribution from the cable to the rubber when the cable is not in tension.

In order to validate free surfaces quantitively, water levels near the right wall are compared in Figure 8 in which water levels due to one-cycle cosine and sine impulses are given in the left and right columns, respectively. Initial water level is 10 cm. The maximum increases in the water levels at the right wall are approximately 24% and 26% for one-cycle cosine and sine impulses, respectively, and observed at the second peak. After the attachment of the cable, the maximum increases in water levels are observed at the first peak. Although the water level increase at the second peak decreases considerably, attachment of the cable does not change water levels at the first peak (at $t = 0.24$ s and $t = 0.30$ s for one-cycle cosine and sine, respectively), noticeably. Maximum decreases in water levels are lowered about 30% and 40% for cosine

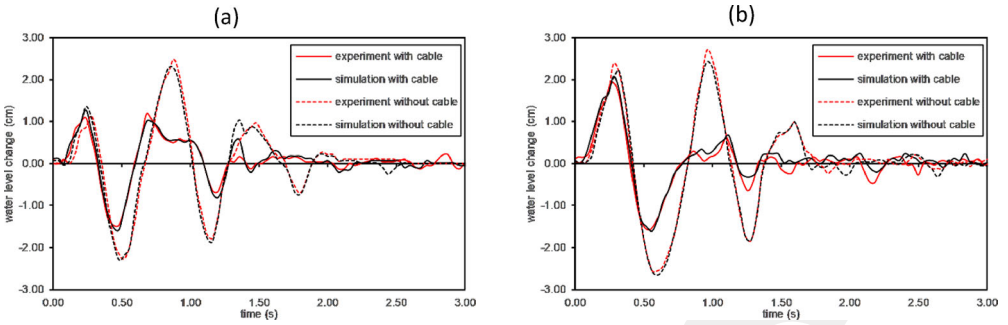

Figure 8. Water level changes near the right wall of (a) one-cycle cosine impulse and (b) one-cycle sine impulse.

and sine impulses, respectively. Figures show that the attachment of the cable lowers the sloshing of the water. In addition, it can be said that numerical model can predict the water levels with high accuracy.

The deformation of the rubber is also important in order to clearly observe the effect of the cable and the accuracy of the numerical model. In Figure 9, the horizontal displacement of the upper right end of the rubber is presented. Maximum horizontal tip displacement under cosine and sine impulses are about 40% and 35%, respectively. When cable elements are attached, tip displacements decrease considerably, i.e. it becomes approximately 10% under cosine impulse and 8.5% in the negative direction under sine impulse. Consequently, maximum tip displacements drop nearly to a quarter when the cable is attached. As it is understood from the figures, numerical method can predict the tip displacement profile of the rubber very well.

In order to analyse the behaviour of the cable quantitively, the tension calculated in the left and the right cables is given in Figure 10. Since the unstretched length of the cable is less than the initial length, a same tension in the left and the right cable is observed at the beginning of the simulation. The tension reaches its initial value, approximately 135 kPa, also at the end of the simulation. When the length of the cable is equal to or less than the unstretched length, a tension due to its own weight is observed. It is as small as nearly 0.25 kPa. The tension due to sine impulse is larger than the tension due to cosine impulse. The time history of tension is consistent with the tip displacement history of the rubber.

Velocity profiles of water particles under cosine and sine impulses when the tip displacements are maximum in both directions are shown in Figures 11 and 12, respectively. In the figures, (a), (b), (c) and (d) denote to the free-surface profile captured from the experiment, velocity distribution in horizontal and vertical directions and velocity vector, respectively. When the tip displacement is maximum in negative direction ($t = 0.40$ s and $t = 0.48$ s for cosine and sine impulses, respectively), the highest magnitudes of velocity for cosine and sine impulses in horizontal direction are 0.35 m/s and 0.60 m/s, and in vertical direction 0.2 m/s and 0.25 m/s, respectively. They are 0.4 m/s and 0.16 m/s in horizontal direction and 0.2 m/s and 0.12 m/s in vertical direction for the maximum tip displacement in positive direction ($t = 0.64$ s and $t = 0.12$ s for cosine and sine impulses, respectively). When maximum tip displacements are in positive horizontal direction, higher magnitudes of velocity are observed for cosine impulse, whereas when they are in negative horizontal direction, magnitudes of velocities are higher due to sine impulse.

The pressures on the right wall 5 mm above the bottom are calculated and given in Figure 13. When δ-SPH model is used, the peak pressures are nearly two times of the initial hydrostatic pressure for both sine and cosine impulses. The peak pressures for the cosine impulse are observed at the beginning of the movement, whereas they are observed approximately at 0.18 and 0.48 s for the sine impulse which are compatible with the input accelerations shown in Figure 4. Although the duration of one-cycle sine and cosine impulses are the same as shown in Figure 4, the pressure due to sine impulse reaches the hydrostatic pressure earlier than the one due to cosine impulse. The numerical results can be validated according to the final pressures which converge to the hydrostatic pressure as expected. When δ-SPH is not implemented, the oscillations in the pressures at the beginning of the simulation are very high. However, oscillations decrease at the later stages of the simulation. Oscillations vanish at $t = 1.00$ s in δ-SPH scheme. On the other hand, when standard SPH equations are used instead of δ-SPH scheme, oscillations are still observed at $t = 1.00$ s under one-cycle cosine impulse. In Figures 14 and 15, the comparison between free-surface profiles of the δ-SPH scheme and the standard SPH is given under cosine

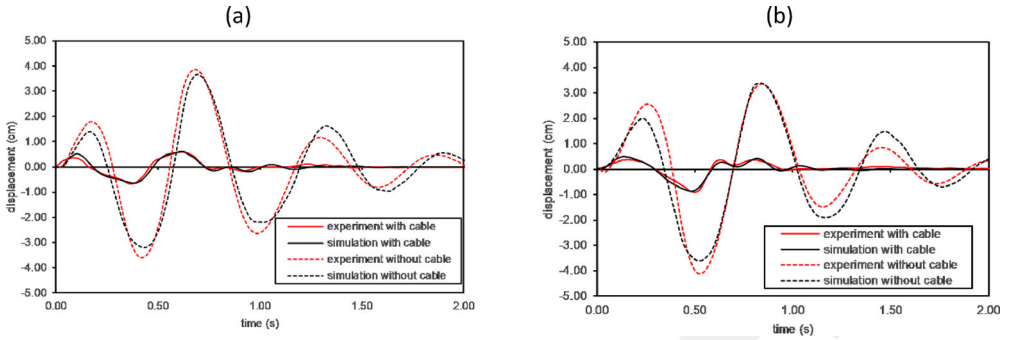

Figure 9. Horizontal tip displacement of the rubber for (a) one-cycle cosine and (b) one-cycle sine impulses.

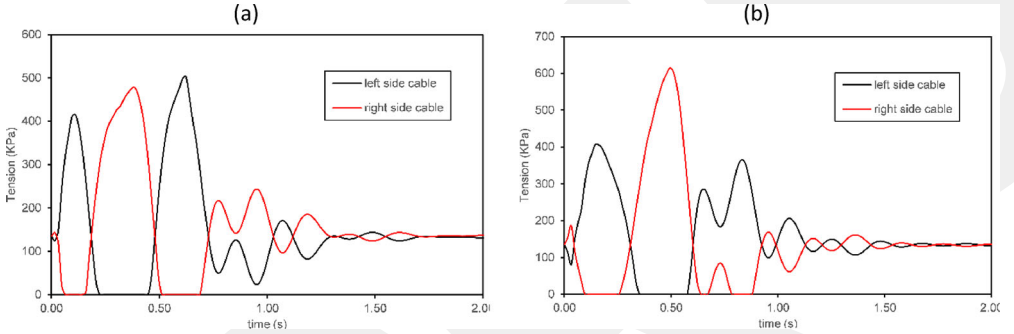

Figure 10. The tension in the cable under (a) one-cycle cosine and (b) one-cycle sine impulses.

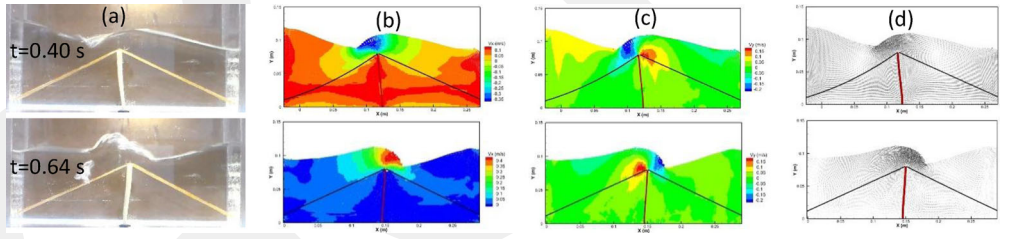

Figure 11. Velocity profiles under one-cycle cosine impulse of (a) experiment and simulation in (b) horizontal direction, (c) vertical direction and (d) resultant velocity.

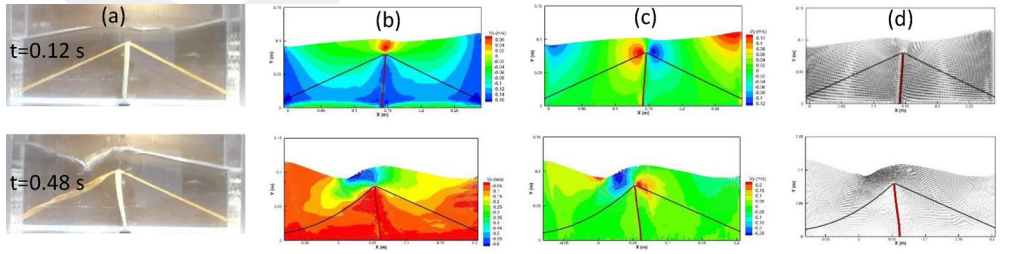

Figure 12. Velocity profiles under one-cycle sine impulse of (a) experiment and simulation in (b) horizontal direction, (c) vertical direction and (d) resultant velocity.

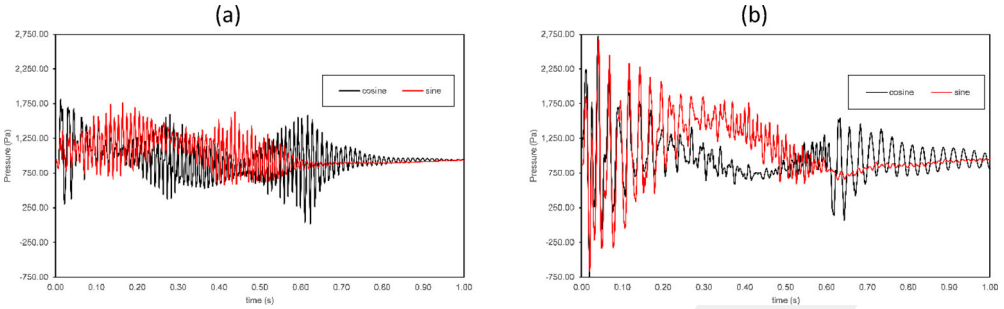

Figure 13. Pressure history under one-cycle cosine and sine impulses of (a) δ-SPH scheme and (b) the standard SPH.

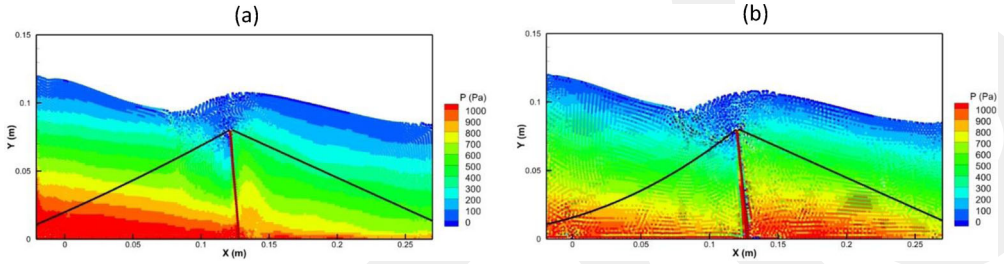

Figure 14. Comparison between free-surface profiles of (a) the δ-SPH scheme and (b) the standard SPH under one-cycle cosine impulse at $t = 0.42$ s.

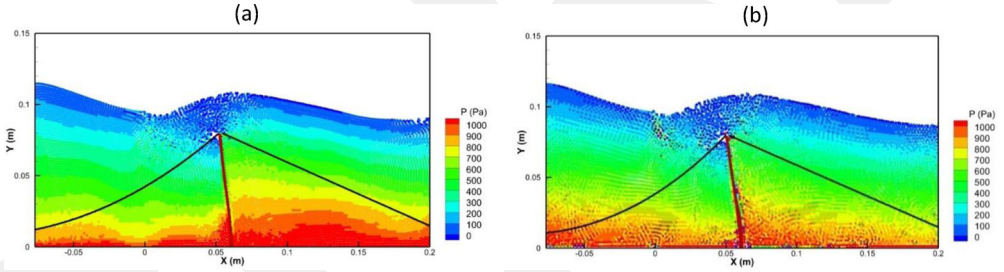

Figure 15. Comparison between free-surface profiles of (a) the δ-SPH scheme and (b) the standard SPH under one-cycle sine impulse at $t = 0.53$ s.

and sine impulses, respectively. As can be seen from the figures, pressure distribution is smoother in δ-SPH scheme.

4.2. Earthquake excitation

Although near-fault-type excitation may damage the structure substantially, submerged structure should also be investigated under earthquake excitation. Since the accelerations on the water tank and rubber change instantaneously during an earthquake, the simulation may be harder. The numerical model is validated under a real earthquake excitation. The 1940 El Centro earthquake occurred in the Imperial Valley in Southern California is used and the corresponding accelerogram is given in Figure 16.

Free-surface profiles due to the 1940 El Centro earthquake for different times which are chosen when the tip displacements of the rubber are the highest can be found in Figure 17. In the figure, left and right column show the experimental and simulation results, respectively. Pressures are colourised in the simulation results. Highest pressures are observed at $t = 1.63$ s and $t = 3.02$ s when the tip displacement of the rubber is maximum in negative and positive horizontal directions, respectively. From the figure, it can be said that the simulated free-surface profiles are in good agreement with the experimental data. In addition, the simulated cable positions are close to the experimental data.

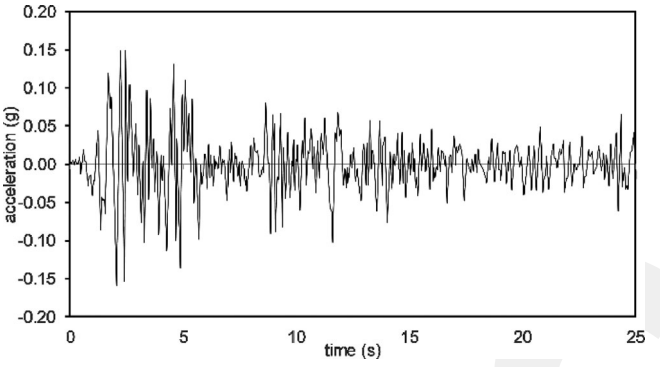

Figure 16. Time history of the 1940 El Centro earthquake.

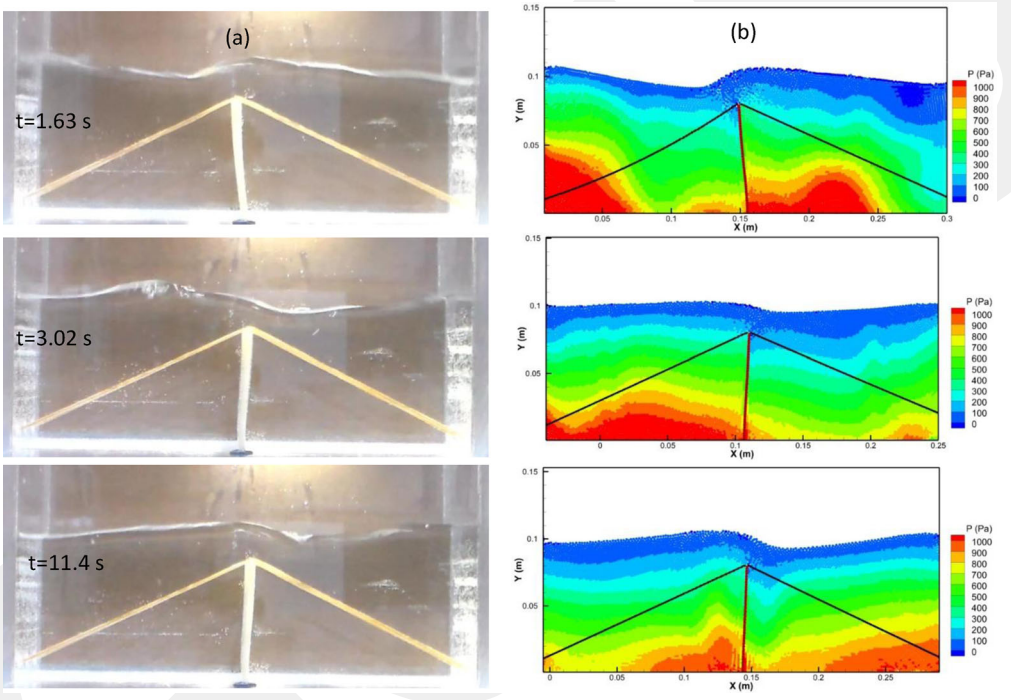

Figure 17. Free-surface profiles under the earthquake for (a) experiment and (b) simulation.

Time history analysis of the horizontal tip displacement of the rubber is shown in Figure 18. In the figure, experimental and numerical results when the upper end of the rubber is free and when the cable is attached are shown. In order to show tip displacements in detail, the figure is divided into two and only the results when the cable is attached are shown in Figure 19. The maximum tip displacement is about 20% of the total length of the rubber when upper end is free. It is approximately 6% when cable is attached to the rubber. Therefore, the tip displacement of the rubber is significantly lowered with the cable element. It should be pointed out that numerical results are very close to the experimental data.

The tension in the cables due to El Centro earthquake is presented in Figure 20. The maximum tension observed in the cable at the initial stages of the simulation is approximately 450 kPa which is lower than the tensions under near-fault excitations although the magnitude of the maximum input accelerations is similar.

The change in water levels near the right wall is given in Figure 21. Maximum changes in water levels are about 20% and 15% when the upper end of the cable is free and cable is attached, respectively.

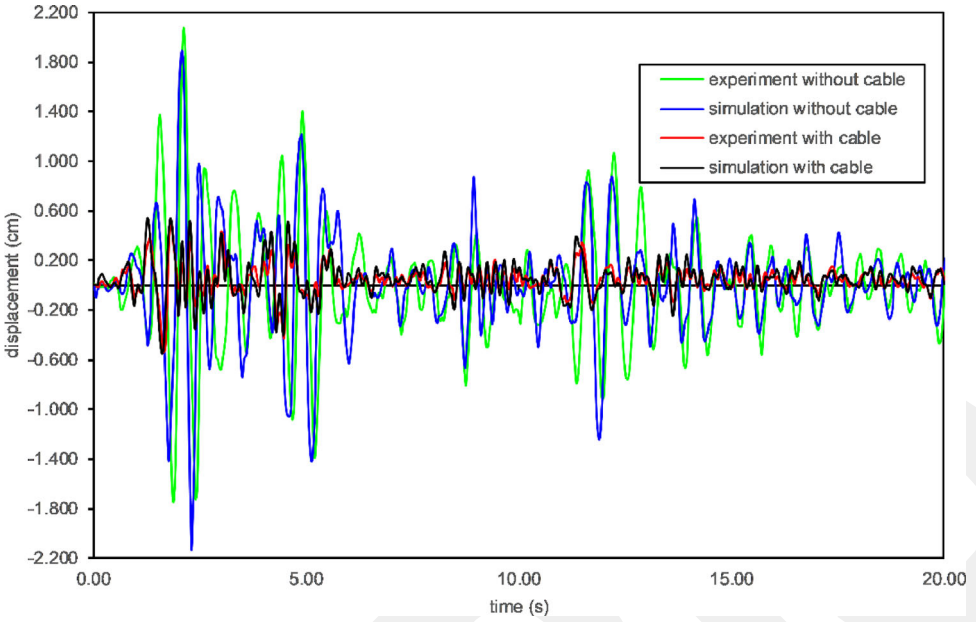

Figure 18. Horizontal tip displacements of the rubber under El Centro earthquake.

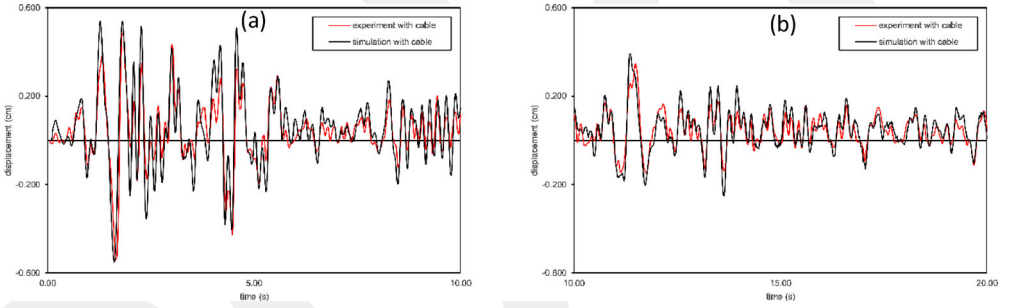

Figure 19. Horizontal tip displacements of the rubber with cable under El Centro earthquake between (a) 0 and 10 s and (b) 10 and 20 s.

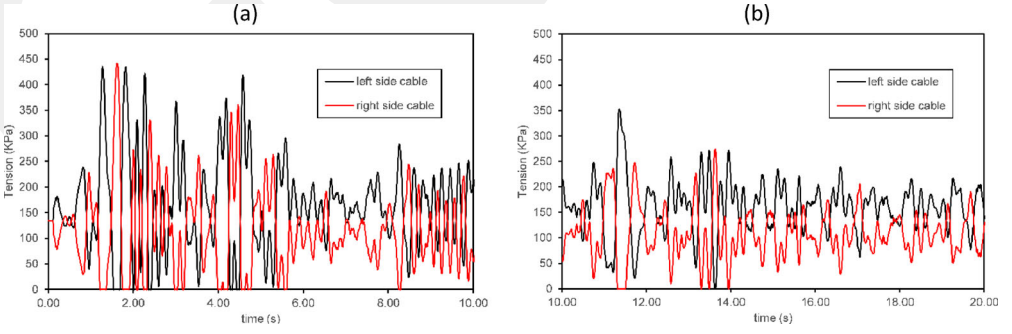

Figure 20. The tension in the cable under El Centro earthquake between (a) 0 and 10 s and (b) 10 and 20 s.

Therefore, it can be deduced that attaching the cable element to the rubber does not decrease the sloshing significantly. In order to compare the numerical results with the experimental data, only the results with the cable are shown in detail in Figure 22. The numerical model can successfully capture the change in water levels.

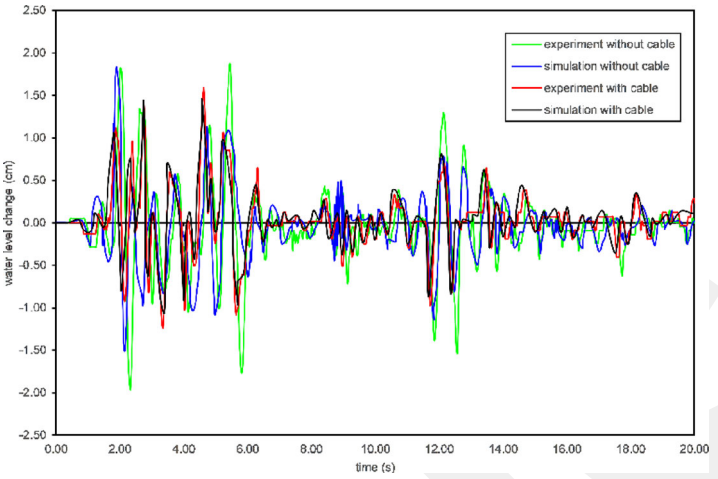

Figure 21. Water level changes near the right wall under El Centro earthquake.

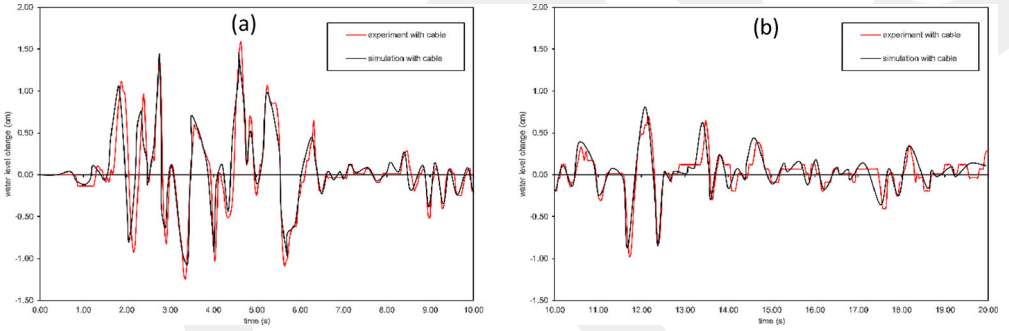

Figure 22. Water level changes near the right wall under El Centro earthquake between (a) 0 and 10 s and (b) 10 and 20 s.

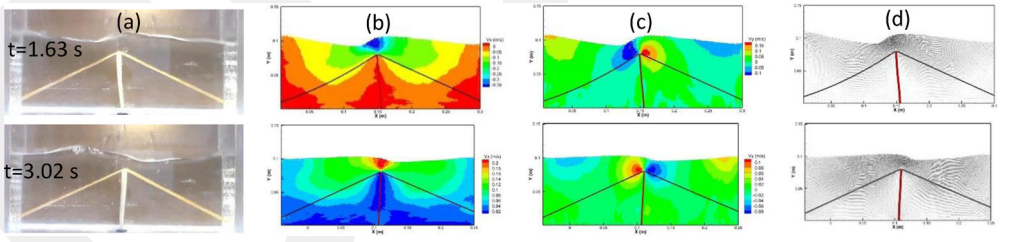

Figure 23. Velocity profiles under El Centro earthquake (a) experiment and simulation in (b) horizontal direction, (c) vertical direction and (d) resultant velocity.

Velocity profiles when the horizontal tip displacements in both directions of the rubber are the highest are given in Figure 23. The highest magnitudes of velocity in horizontal direction are 0.3 and 0.2 m/s when the tip displacement is in the negative and positive directions, respectively. In vertical direction, they are found to be 0.15 and 0.1 m/s. Although the tip displacements in both directions are close to each other as can be seen in Figure 19, the magnitudes of velocity vectors are different. The velocity when the tip displacement is in negative direction is nearly 1.5 times the velocity found when the tip displacement is in positive direction.

The pressure history at the right wall 5 mm above the bottom until reaching the steady flow can be seen in Figure 24. The peak pressure is obtained approximately at 1.80 s after the beginning of the

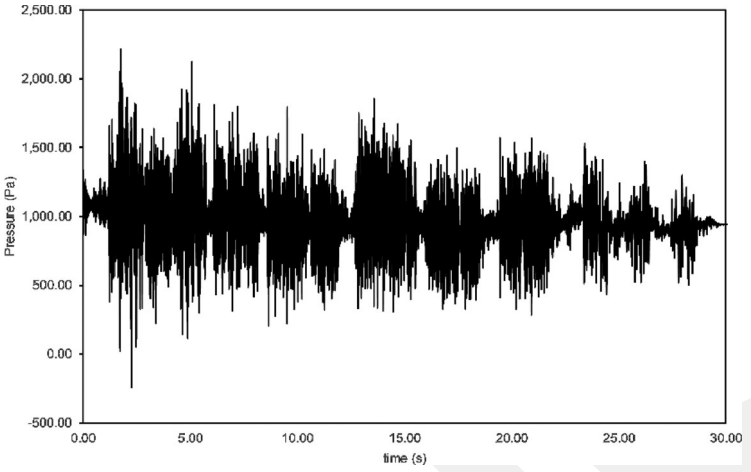

Figure 24. Pressure history under El Centro earthquake.

Table 2. Error measurements for near-fault excitations.

		One-cycle cosine impulse		One-cycle sine impulse	
		With cable	Without cable	With cable	Without cable
Error in peak displacement (%)	Peak 1	16.28	21.35	32.43	16.74
	Peak 2	1.52	11.67	2.25	12.59
	Peak 3	1.69	5.71	20.59	1.20
	Average	6.50	12.91	18.42	10.17
Error in time to peak displacement (%)	Peak 1	20.00	11.11	18.75	4.35
	Peak 2	5.56	4.76	2.08	1.89
	Peak 3	1.33	0.00	1.56	1.18
	Average	8.96	5.29	7.47	2.47
Error in peak water level on the right wall (%)	Peak 1	15.45	20.35	7.25	6.75
	Peak 2	7.48	1.77	0.63	3.92
	Peak 3	16.10	7.69	6.45	10.37
	Average	13.01	9.94	4.78	7.01
Error in time to peak water level on the right wall (%)	Peak 1	0.00	14.29	7.69	14.29
	Peak 2	0.00	7.69	3.70	3.45
	Peak 3	0.00	2.27	1.82	0.00
	Average	0.00	8.08	4.40	5.91

simulation and it is nearly 2.5 times the initial hydrostatic pressure at that point. As can be seen in Figure 16, the maximum input acceleration is observed nearly at the same time when the peak pressure occurs. Pressures oscillate due to the movement of the tank around the hydrostatic pressure to which they reach at the end of the sloshing motion.

4.3. Error analysis

Error measurements of simulations for the first three peaks are given in Table 2. The numerical differences between simulations and experiments in terms of peak displacements, time to peak displacements, peak water levels on the right wall and time to peak water levels on the right wall are presented in the table. The highest errors are usually observed at the first peak. After the first peak, the errors decrease significantly. In fact, the difference between numerical and experimental results can also be seen in Figures 8 and 10. Except from the peak displacements, average errors are generally below 10%.

5. Conclusions and future work

A cable model is incorporated with the fully coupled SPH-FE method previously proposed by the author (Dinçer et al., 2019) and the behaviour of a highly elastic submerged structure as well as the sloshing of

the water under seismic excitations are investigated. The liquid sloshing height near one of the walls of the water tank, the tip displacements of the rubber representing the elastic submerged structure, the free surfaces of the water and the tensions in the cable due to near-fault and earthquake excitations are discussed, the conclusions are as follows:

First, although the peak acceleration impulses of El Centro earthquake and near-fault motions are close to each other, the tip displacement of the submerged rubber is approximately 20% and 40% of its initial height, respectively. Near-fault excitation is far more destructive than an earthquake excitation with the same peak acceleration. When a highly elastic cable element is attached to the rubber, tip displacements become 6% and 10%, respectively. Therefore, cable significantly decrease the displacement of the rubber.

Second, attaching a cable element to the rubber does not lower the sloshing of the water in the tank significantly for the earthquake excitation. On the other hand, for the near-fault excitations, maximum sloshing height is lowered with the cable although sloshing heights at the first peak with and without cable are very close.

Third, the magnitudes of the velocity of the water particles due to near-fault excitations are nearly twice the ones due to earthquake excitation. Besides, the peak pressures recorded at the bottom of the right wall due to one-cycle cosine and sine impulses are very close to each other and found to be approximately two times of the initial hydrostatic pressure at the measurement point. However, peak pressure due to El Centro earthquake is about three times of the hydrostatic pressure. Pressures at the end of the sloshing of the water reach the constant hydrostatic pressure and they do not oscillate significantly.

Instead of using closed form solutions, a comprehensive finite element method with a two-node cable element is implemented in the proposed FSI method. Simulation results show that the proposed model can successfully simulate the behaviour of an idealised, submerged structure with a cable element. Besides, the free surfaces of the water and the positions of the cable elements at different instants are also captured correctly. It should be pointed out that in order to validate the numerical model derived for this study, novel experiments are conducted and these experiments may be the benchmark for complex FSI problems including cable elements.

The current version of the proposed numerical model still presents some limitations. The interaction between the cable and water is ignored. However, the calculated and recorded positions of the cable are close to each other. Future work will be focussed on the interaction of the cable with the fluid. In order to compare the numerical and experimental results quantitively, the tension in the cable will also be measured.

Disclosure statement

No potential conflict of interest was reported by the author(s).

ORCID

A. Ersin Dinçer http://orcid.org/0000-0002-4662-894X

References

Adami, S., Hu, X. Y., & Adams, N. A. (2012). A generalized wall boundary condition for smoothed particle hydrodynamics. *Journal of Computational Physics, 231*(21), 7057–7075. https://doi.org/10.1016/j.jcp.2012.05.005

Akbarian, E., Najafi, B., Jafari, M., Ardabili, S. F., Shamshirband, S., & Chau, K. W. (2018). Experimental and computational fluid dynamics-based numerical simulation of using natural gas in a dual-fueled diesel engine. *Engineering Applications of Computational Fluid Mechanics*, *12*(1), 517–534. https://doi.org/10.1080/19942060.2018.1472670

Anderson, J. D. (1995). *Computational fluid dynamics: The basics with applications*. McGraw-Hill.

Antoci, C., Gallati, M., & Sibilla, S. (2007). Numerical simulation of fluid-structure interaction by SPH. *Computers and Structures, 85*(11–14), 879–890. https://doi.org/10.1016/j.compstruc.2007.01.002

Antuono, M., Colagrossi, A., Marrone, S., & Molteni, D. (2010). Free-surface flows solved by means of SPH schemes with numerical diffusive terms. *Computer Physics Communications*, *181*(3), 532–549. https://doi.org/10.1016/j.cpc.2009.11.002

Barreiro, A., Crespo, A. J. C., Dominguez, J. M., Garcia-Feal, O., Zabala, I., & Gomez-Gesteira, M. (2016). Quasi-static mooring solver implemented in SPH. *Journal of Ocean Engineering and Marine Energy*, *2*(3), 381–396. https://doi.org/10.1007/s40722-016-0061-7

Bathe, K.-J., & Chaudhary, A. (1985). A solution method for planar and axisymmetric contact problems. *International Journal for Numerical Methods in Engineering*, *21*(1), 65–88. https://doi.org/10.1002/nme.1620210107

Blanc, T., & Pastor, M. (2011). Towards sph modelling of failure problems in geomechanics: A fractional step Taylor-sph model. *European Journal of Environmental and Civil Engineering, 15*(Suppl. 1), 31–49. https://doi.org/10.1080/19648189.2011.9695303

Calderer, A., Kang, S., & Sotiropoulos, F. (2014). Level set immersed boundary method for coupled simulation of air/water interaction with complex floating structures. Journal of Computational Physics, 277, 201–227. https://doi.org/10.1016/j.jcp.2014.08.010

Cao, X. Y., Ming, F. R., & Zhang, A. M. (2014). Sloshing in a rectangular tank based on SPH simulation. *Applied Ocean Research, 47*, 241–254. https://doi.org/10.1016/j.apor.2014.06.006

Colagrossi, A., & Landrini, M. (2003). Numerical simulation of interfacial flows by smoothed particle hydrodynamics. *Journal of Computational Physics, 191*(2), 448–475. https://doi.org/10.1016/S0021-9991(03)00324-3

Crespo, A. J. C., Altomare, C., Domínguez, J. M., González-Cao, J., & Gómez-Gesteira, M. (2017). Towards simulating floating offshore oscillating water column converters with Smoothed Particle Hydrodynamics. *Coastal Engineering, 126*, 11–26. https://doi.org/10.1016/j.coastaleng.2017.05.001

Cui, J., Li, Q., Cheng, Y., Ji, C. Y., & Deng, X. K. (2019). Addition of dynamic mooring line force based on lumped-mass method in SPH. *Ocean Engineering*, *182*, 90–101. https://doi.org/10.1016/j.oceaneng.2019.04.006

Cyril, P. A., Kok, S. T., Song, M. K., Chan, A., Wong, J. Y., & Choong, W. K. (2019). Smooth particle hydrodynamics for the analysis of stresses in soil around Jack-in Pile. *European Journal of Environmental and Civil Engineering,* 1–27. https://doi.org/10.1080/19648189.2019.1649198

Davidson, J., & Ringwood, J. V. (2017). Mathematical modelling of mooring systems for wave energy converters – A review. *Energies*, *10*(5), 666. https://doi.org/10.3390/en10050666

Dehnen, W., & Aly, H. (2012). Improving convergence in smoothed particle hydrodynamics simulations without pairing instability. Monthly Notices of the Royal Astronomical Society, *425*(2), 1068–1082. https://doi.org/10.1111/j.1365-2966.2012.21439.x

Demir, A., Dinçer, A. E., Bozkus, Z., & Tijsseling, A. S. (2019). Numerical and experimental investigation of damping in a dam-break problem with fluid-structure interaction. *Journal of Zhejiang University-Science A*, *20*(4), 258–271. https://doi.org/10.1631/jzus.A1800520

Dinçer, A. E. (2017). *Numerical investigation of free surface and pipe flow problems by smoothed particle hydrodynamics* [thesis]. The Graduate School of Natural and Applied Sciences of Middle East Technical University.

Dinçer, A. E. (2019). Investigation of the sloshing behavior due to seismic excitations considering two-way coupling of the fluid and the structure. *Water*, *11*(12), 2664. https://doi.org/10.3390/w11122664

Dinçer, A. E., Bozkuş, Z., & Tijsseling, A. S. (2018). Prediction of pressure variation at an elbow subsequent to a liquid slug impact by using smoothed particle hydrodynamics. *Journal of Pressure Vessel Technology*, *140*(3), 031303. https://doi.org/10.1115/1.4039696

Dinçer, A. E., Demir, A., Bozkus, Z., & Tijsseling, A. S. (2019). Fully coupled smoothed particle hydrodynamics-finite element method approach for fluid-structure interaction problems with large deflections. *Journal of Fluids Engineering, Transactions*, *141*, 1–13. https://doi.org/10.1115/1.4043058

Fogazzi, P., & Perotti, F. (2000). The dynamic response of seabed anchored floating tunnels under seismic excitation. *Earthquake Engineering & Structural Dynamics*, *29*(3), 273–295. https://doi.org/10.1002/(SICI)1096-9845(200003)29:3<273::AID-EQE899>3.0.CO;2-Z

Ghalandari, M., Bornassi, S., Shamshirband, S., Mosavi, A., & Chau, K. W. (2019). Investigation of submerged structures' flexibility on sloshing frequency using a boundary element method and finite element analysis. *Engineering Applications of Computational Fluid Mechanics, 13*(1), 519–528. https://doi.org/10.1080/19942060.2019.1619197

Gingold, R. A., & Monaghan, J. J. (1977). Smoothed particle hydrodynamics: Theory and application to non-spherical stars. *Monthly Notices of the Royal Astronomical Society, 181*(3), 375–389. https://doi.org/10.1093/mnras/181.3.375

Gomez-Gesteira, M., Rogers, B. D., Dalrymple, R. A., & Crespo, A. J. C. (2010). State-of-the-art of classical SPH for free-surface flows. *Journal of Hydraulic Research, 48*(Suppl.1), 6–27. https://doi.org/10.1080/00221686.2010.9641242

Kim, N. H., Park, Y. H., & Choi, K. K. (2001). Optimization of a hyper-elastic structure with multibody contact using continuum-based shape design sensitivity analysis. *Structural and Multidisciplinary Optimization*, *21*(3), 196–208. https://doi.org/10.1007/s001580050184

Liu, G. R., & Liu, M. B. (2003). *Smoothed particle hydrodynamics, a meshfree particle method* (1st ed.). World Scientific Publishing Co. Pte. Ltd.

Liu, M. B., & Liu, G. R. (2010). Smoothed particle hydrodynamics (SPH): An overview and recent developments. *Archives of Computational Methods in Engineering*, *17*(1), 25–76. https://doi.org/10.1007/s11831-010-9040-7

Lucy, L. B. (1977). A numerical approach to the testing of the fission hypothesis. *The Astronomical Journal*, *82*, 1013–1024. https://doi.org/10.1086/112164

Marrone, S., Antuono, M., Colagrossi, A., Colicchio, G., Le Touzé, D., & Graziani, G. (2011). δ-SPH model for simulating violent impact flows. *Computer Methods in Applied Mechanics and Engineering, 200*(13–16), 1526–1542. https://doi.org/10.1016/j.cma.2010.12.016

Monaghan, J. J. (1994). Simulating free surface flows with SPH. *Journal of Computational Physics*, *110*(2), 399–406. https://doi.org/10.1006/jcph.1994.1034

Monaghan, J. J. (2000). SPH without a tensile instability. *Journal of Computational Physics*, *159*(2), 290–311. https://doi.org/10.1006/jcph.2000.6439

Monaghan, J. J., & Kos, A. (1999). Solitary waves on a Cretan beach. *Journal of Waterway, Port, Coastal, and Ocean Engineering, 125*(3), 145–155. https://doi.org/10.1061/(ASCE)0733-950X(1999)125:3(145)

Morris, J. P., Fox, P. J., & Zhu, Y. (1997). Modeling low Reynolds number incompressible flows using SPH. *Journal of Computational Physics*, *136*(1), 214–226.

Nakajima, T. (1982). On the *dynamic analysis of multi-component mooring lines* [Paper presentation]. Proceedings of 14th Annual Offshore Technology Conference, Houston, TX (pp. 105–120). https://doi.org/10.4043/4309-MS

Newmark, N. M. (1959). A method of computation for structural dynamics. *Journal of Engineering Mechanics Division*, *85*, 67–94.

Orgill, G., Wilson, J. F., & Schmertmann, G. R. (1985). Static design of cable mooring arrays for offshore guyed towers. *Applied Ocean Research,* 7(3), 166–174. https://doi.org/10.1016/0141-1187(85)90009-4

Rebouillat, S., & Liksonov, D. (2010). Fluid-structure interaction in partially filled liquid containers: A comparative review of numerical approaches. *Computers & Fluids, 39*(5), 739–746. https://doi.org/10.1016/j.compfluid.2009.12.010

Ren, B., He, M., Li, Y., & Dong, P. (2017). Application of smoothed particle hydrodynamics for modeling the wave-moored floating breakwater interaction. *Applied Ocean Research*, *67*, 277–290. https://doi.org/10.1016/j.apor.2017.07.011

Shao, J. R., Li, H. Q., Liu, G. R., & Liu, M. B. (2012). An improved SPH method for modeling liquid sloshing dynamics. *Computers and Structures, 100–101*, 18–26. https://doi.org/10.1016/j.compstruc.2012.02.005

Wai Li, C., & Busari, A. O. (2019). Hybrid modeling of flows over submerged prismatic vegetation with different areal densities. *Engineering Applications of Computational Fluid Mechanics, 13*(1), 493–505. https://doi.org/10.1080/19942060.2019.1610501

Yang, Q., Jones, V., & McCue, L. (2012). Free-surface flow interactions with deformable structures using an SPH-FEM model. *Ocean Engineering*, *55*, 136–147. https://doi.org/10.1016/j.oceaneng.2012.06.031

Yang, Y. B., & Tsay, J.-Y. (2007). Geometric nonlinear analysis of cable structures with a two-node cable element by generalized displacement control method. *International Journal of Structural Stability and Dynamics*, *7*(4), 571–588. https://doi.org/10.1142/S0219455407002435

Zhang, S., & Wang, G. (2013). Effects of near-fault and far-fault ground motions on nonlinear dynamic response and seismic damage of concrete gravity dams. *Soil Dynamics and Earthquake Engineering*, *53*, 217–229. https://doi.org/10.1016/j.soildyn.2013.07.014

Zhu, X. Q., Yoo, W. S., & Bauchau, O. A. (2013). Dynamic analysis of mooring cable fastening a floating sphere on the ocean [Paper presentation]. ASME 2013 International Design Engineering Technical Conferences and Computers and Information in Engineering Conference, IDETC/CIE 2013, Portland, OR. https://doi.org/10.1115/DETC2013-12693